DOI 10.1007/s10946-015-9537-5
Journal of Russian Laser Research, Volume 36, Number 6, November, 2015

DYNAMICAL BRAGG DIFFRACTION IN THE LAUE GEOMETRY IN 1D POROUS SILICON-BASED PHOTONIC CRYSTALS

Sergey E. Svyakhovskiy,[1*] Anton I. Maydykovskiy,[1] Vladimir B. Novikov,[1] Viktor O. Kompanets,[2] Aleksandr A. Skorynin,[1] Vladimir A. Bushuev,[1] Sergey V. Chekalin,[2] Tatiana V. Murzina,[1] and Boris I. Mantsyzov[1]

[1] *Faculty of Physics*
Lomonosov Moscow State University
Leninskie Gory, Moscow 119992, Russia

[2] *Institute of Spectroscopy, Russian Academy of Sciences*
Troitsk, Moscow Region 142092, Russia

*Corresponding author e-mail: sse@shg.ru

Abstract

We consider optical effects accompanying the dynamical Bragg diffraction in the Laue geometry in one-dimensional photonic crystals (PhC). We predict theoretically, and observe in the experiment, the diffraction-induced pulse splitting of femtosecond light pulse, the optical switching due to the optical pendular effect, and the effects of selective compression and focusing. These effects originate from the interaction of two spatial eigenmodes of the photonic crystal: Borrmann and anti-Borrmann, which are spatially localized within a PhC in the layers with low and high dielectric constants, respectively.

Keywords: dynamical diffraction, photonic crystals, Laue geometry, femtosecond phenomena, pulse shaping, optical switching, porous silicon.

1. Introduction

The control of light propagation at small scales of time and space is a promising development nowadays. Photonic crystals (PhC), being spatially periodic dielectric structures, have several advantages such as low losses, scalability, and integration to optical chips [1]. They reveal plenty of optical effects enabling the control of the light propagation: modulation of the spontaneous emission decay known as the Purcell effect [2, 3], extremely low group velocity [4, 5], an enhancement of the linear and nonlinear effects like the second-harmonic generation [6], Raman scattering [7], magneto-optical effects [8], etc.

The dynamical Bragg diffraction of light in a PhC is a subject of extensive research [9]. The Laue transmission geometry can reveal the dynamical diffraction effects by means of the interaction of two spatial modes, the so-called Borrmann and anti-Borrmann modes [10], which are localized inside a PhC in the layers of low and high dielectric constants, respectively. This brings about different group velocities and dispersion of these modes, which provides selective control over the mode propagations within a PhC. The interaction of the Borrmann and anti-Borrmann modes leads to a number of specific effects, such as

Manuscript submitted by the authors in English on August 3, 2015.

the Borrmann phenomenon, pendular effect [11], diffraction-induced pulse splitting (DIPS) [12], second-harmonic generation [13].

In this paper, we discuss our recent theoretical and experimental results on the dynamical diffraction of short light pulses in 1D PhC.

This paper is organized as follows.

In Sec. 2, we present the theory of diffraction-induced pulse splitting. In Sec. 3, we describe the production technique of the 1D porous silicon PhC. We devote Sec. 4 to the experimental observation of the DIPS effect, and we discuss its polarization properties in Sec. 5. We demonstrate the control over the spatial pulse propagation in Sec. 6, deal with the diffraction of phase-modulated pulses in Sec. 7, and consider the optical pendular effect in Sec. 8. Finally, we give our summary in Sec. 9.

2. Diffraction-Induced Pulse Splitting: the Theory

We consider a one-dimensional photonic crystal as an array of alternating layers of two types with refractive indices of n_1 and n_2, and thicknesses of d_1 and d_2, respectively [10]. The sketch of the geometry is shown in Fig. 1 a. The number of layers in the x direction is considered infinite. The length of the crystal is z_0. The electric field of the incident optical pulse can be represented as a wave packet

$$\mathbf{E}_{\text{in}}(\mathbf{r},t) = \mathbf{e}_{\text{in}} E_{\text{in}}(\mathbf{r},t)\exp(i\mathbf{k}_{\text{in}}\mathbf{r} - i\omega_0 t), \tag{1}$$

where E_{in} is a slowly varying complex amplitude, $\mathbf{k}_{\text{in}}$ is the wave vector, $\omega_0 = 2\pi c/\lambda_0$ is the central frequency of the pulse, λ_0 is its central wavelength, and $\mathbf{e}_{\text{in}}$ is a unit vector. The pulse enters the PhC at the Laue geometry under the angle of incidence θ that matches the Bragg diffraction condition $\lambda_0 = 2d\sin\theta$, where $d = d_1 + d_2$ is a spatial period of the structure. All the electromagnetic waves inside the PhC obey the wave equation

$$\nabla \times \nabla \times \mathbf{E}(\mathbf{r},t) + \frac{\varepsilon(x)}{c^2}\frac{\partial^2 \mathbf{E}(\mathbf{r},t)}{\partial t^2} = 0, \tag{2}$$

where $\varepsilon(x) = n^2(x)$ is a periodically modulated permittivity of the PhC. The initial pulse can be Fourier-transformed to a set of plane waves; then we solve Eq. (2) for each plane wave with the wave vector $\mathbf{k}$, taking into account the boundary conditions $k_x = q_{x,0}$ and $k_x - h = q_{x,h}$ for the transmitted and diffracted waves, respectively. Here, h is the amplitude of the PhC reciprocal-lattice vector.

Generally, there are two solutions $\mathbf{q}_0^{(1,2)}$ for the transmitted wave and the two solutions $\mathbf{q}_h^{(1,2)}$ for the diffracted wave. The solution [10, 14] of the wave equation with smaller wave vector is called the Borrmann mode, while the one with the larger wave vector is called the anti-Borrmann mode. For each wave vector, there are two solutions that match the Bragg condition and the finite spectral width of the incident pulse

$$\Delta\omega < \frac{\omega_0|\varepsilon_h|}{2\sin^2\theta_B}, \tag{3}$$

so this solution exits for pulses with limited spectral width. The value of ε_h is the spatial Fourier amplitude of the permittivity, and $\varepsilon(x)$ is proportional to the refractive index contrast Δn.

The scheme of the DIPS effect is shown in Fig. 1 a. The incident beam enters the PhC at the Bragg angle. Within the PhC, each part of the pulse is split into two components corresponding to the Borrmann and anti-Borrmann modes. Since the Borrmann mode has larger group velocity and propagates faster

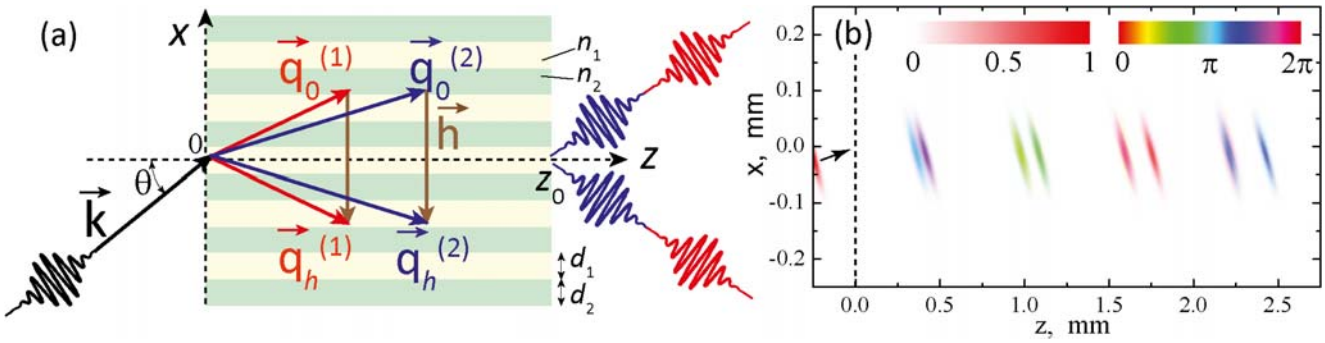

Fig. 1. Scheme of the dynamical diffraction in the Laue geometry and of the effect of diffraction-induced pulse splitting, where red wave vectors and pulses correspond to the Borrmann mode, blue ones correspond to the anti-Borrmann mode, and black ones correspond to the initial pulse (a). Results of the analytical calculations of the complex envelope of the pulse propagating through the PhC for the following parameters: $n_1 = 1.48$, $n_2 = 1.32$, $d_1 = d_2 = 400$ nm, $\theta = 30°$, $\lambda_0 = 800$ nm, and $\tau = 100$ fs (b). The phase is shown by the color and the amplitude by the color saturation.

than the anti-Borrmann one, the incident pulse can be split into two consequent pulses when passing through a PhC. This is illustrated by the calculations based on previously described theory [14,15] and is shown in Fig. 1 b. The incident pulse is split into two pulses; the splitting time t_{12} increases linearly with the propagation distance z and the refractive index contrast $\Delta n \sim \varepsilon_h$ as $t_{12} = (z\varepsilon_h/c\sqrt{\varepsilon_0})(1-\sin^2\theta_B/2\varepsilon_0)$, where ε_0 is the average permittivity. Therefore, in order to observe the DIPS effect, both high refractive-index contrast and a large thickness of the PhC are required.

Table 1. Estimation of the Splitting Depth z_{DIPS} of the Ti : Sapphire Optical Pulse ($\tau_0 = 100$ fs, $\lambda = 800$ nm) in PhCs Produced by Currently Available Techniques.[a]

Periodic structure	Reference	Δn	z_{DIPS}	$z_{\max}$
Kerr nonlinear optical lattice	[16, 17]	$6 \cdot 10^{-4}$	50 cm	10 cm
Acousto-optic lattice	[18]	10^{-3}	40 cm	2.5 cm
Laser micropatterning of SiO_2	[19]	$2 \cdot 10^{-3}$	20 cm	1.1 cm
Photo-polymerization	[20, 21]	0.12	1 mm	0.2 mm
Artificial opal	[22]	0.2	1200 μm	500 μm
Colloid crystals	[23, 24]	0.1	500 μm	1 cm*
Porous silicon	[25]	0.5	100 μm	1 cm
Sputter coating	[26]	1	50 μm	$>$ 1 cm*
Plasma etching	[27]	1	50 μm	$>$ 1 cm*

[a]Here, Δn is the refractive index contrast and $z_{\max}$ is the sample length technology limited. Techniques marked with the star are discussed in the text.

We have performed a comparative study of currently available technologies of photonic crystal production; the results are summarized in Table 1. The DIPS effect can be observed if the incident pulse of duration τ_0 is split with splitting time $t_{12} = 2\tau_0$. The corresponding passing length in a PhC is called the splitting depth z_{DIPS}.

For typical values of the refractive index contrast Δn and a standard Ti : Sapphire laser system,

the value of z_{DIPS} was theoretically calculated and compared with the PhC length $z_{\max}$ available for a particular technology. It stems from Table 1 that the most surveyed technologies cannot provide sample lengths large enough for the observation of the DIPS effect. The most popular way to produce 1D photonic crystals is the sputtering of multilayer dielectric coatings and fulfills the requirements for $z_{\max}$, while cannot guarantee a sufficient size in the x direction (see Fig. 1), as the number of layers is limited to several tens. The plasma etching of a substrate using a lithographic mask allows one to produce PhC samples with a large number of periods and $z_{\max}$ but is limited in the y direction. Artificial opals can provide sufficient geometrical sizes, while they are polycrystalline and contain usually some defects. So one may conclude that the porous silicon-based PhC fabrication technique is suitable for the observation of diffraction-induced pulse splitting. We describe it in the next section.

3. Porous Silicon and Porous Fused Silica Photonic Crystals

The experimental studies of the dynamical diffraction in PhCs need to produce samples of hundreds of periods while keeping a high structural quality of a PhC. In our work, we made the PhCs using a modified technique of electrochemical etching of crystalline silicon [28]. It is known that anodization of a Si wafer in HF solution leads to the formation of a porous layer [29]. The direction of pores depends on the crystallographic index of the Si surface and is normal to the surface in the case of Si (001) [25]. The depths of the pores are almost equal [30]. The average diameter of pores depends on the anodic current density [31] and since that can be easily controlled. Therefore, periodic (in time) modulation of the anodic current leads to a periodic space modulation of porosity. The application of the alternating currents of two values causes the formation of two periodically alternating layers of various porosity and, thus, of different refractive indices, thus forming a 1D PhC [32].

The sample was made by electrochemical etching technique from a boron-doped p-Si (001) wafer with a resistivity of 0.005 $\Omega \cdot$cm by application of alternating current densities of $j_1 = 40$ mA/cm^2 and $j_2 = 200$ mA/cm^2 and using the $\mathrm{HF} : \mathrm{H_2O} : \mathrm{C_2H_5OH}$ solution (21 : 21 : 58 w/w) as an electrolyte. The thickness of each layer was 400±10 nm. The SEM image of the PhC structure is shown in Fig. 2 a. A multilayer structure with layer thicknesses approximately 400 nm can be clearly seen, the pore width being about 50 nm, as is clear from the inset in Fig. 2 a. The estimated porosity of the (volume fraction of voids) is about 50%. The number of the alternating layers in the PhC sample was 750. After the final layer of the PhC was made, the structure was split from the substrate (remaining bulk silicon) by a high-current pulse (about 600 mA/cm^2).

The refractive indices of the porous silicon layers were determined independently — two single-layer samples of the same porosity as those in the PhC sample with a thickness of 10 μm were made. Their refractive indices were estimated from the interference patterns and the values obtained are $n_1 = 2.26$ and $n_2 = 1.64$ at 800 nm. Corresponding values of porosity are $p_1 = 49\%$ and $p_2 = 64\%$.

The reflectance spectra of the front PhC side (layers made at the very beginning of the etching process) and of the back side (the last made layers) are shown in Fig. 2 b. The spectra consist of nearly zero plateau and reflectance maxima corresponding to the 7th, 6th, 5th, and 4th photonic band gaps. The maxima attained for the front and back sides reveal very close spectral positions, even for the high-order band gaps, which indicates the good quality of the multilayer structure.

Since silicon is not transparent for the visible light, we performed thermal oxidation of the porous silicon to form the porous fused silica ($\mathrm{SiO_2}$). The annealing was performed in air at a temperature of 900°C for 2 h. The thermal oxidation of silicon under these conditions can be controlled by choosing the

temperature and duration of annealing, because this process is limited by the diffusion of oxygen through the oxide layer [33]. Under our conditions, the thickness of the oxide layer calculated by the Deal–Grove oxidation model [33] is about 25 nm. This value is equal to the half-distance between two pores, so the oxidation process occurs in the whole volume of the sample starting from the surface of pores and until the overlapping of the oxide layers of neighbor pores.

The reflectance spectra of the sample after the thermal annealing are shown in Fig. 2 c. Similarly to that described above, the spectrum of the front side has the same maxima as the spectrum of the back side; therefore, the PhC remains after the annealing. The maxima corresponding to the 5th, the 4th, and the 3th band gaps can be seen. It can be also seen that the annealing leads to a spectral shift of the band-gap structure, because the refractive indices of porous SiO_2 layers are lower than of the corresponding porous Si layers. Measured by the interference patterns on uniform single-layer samples, the values are $n_1 = 1.48$ and $n_2 = 1.32$. The physical thickness of the sample and all layers remains almost the same — the relative change is less than 5%.

Thus, we showed that the electrochemical etching technique followed by thermal annealing allows us to produce the transparent multilayer structures of porous SiO_2 with high refractive index contrast ($\Delta n > 0.1$) and high number of periods (up to 2500) simultaneously.

4. Experimental Studies of the Diffraction-Induced Pulse Splitting

The experimental set-up used for the studies of the dynamical Bragg diffraction of femtosecond laser pulses is shown schematically in Fig. 3 a. As a light source, a Ti : Sapphire laser (Avesta inc, mean power 300 mW, central wavelength 800 nm, pulse duration 40 fs, repetition rate 80 MHz) was used. The fundamental beam was split into two "arms" – the reference arm and the sample arm in a proportion of 20 : 80. Both arms contained the delay lines and four-prism pulse compressors. The compressor in the reference arm was adjusted for the minimum pulse width of approximately 25 fs, and the compressor in the signal arm could be tuned to provide a pulse of 35–140 fs, positive or negative chirp. The polarization in the sample arm could be controlled by two half-wave plates placed in the plane front sections of the beam track before and after the focusing elements. The radiation in the sample arm was focused on the PhC facet into a spot of 20 μm in diameter. The beam passed through the sample was collected by a parabolic mirror and superposed with the reference beam in a nonlinear crystal (BBO). The non-

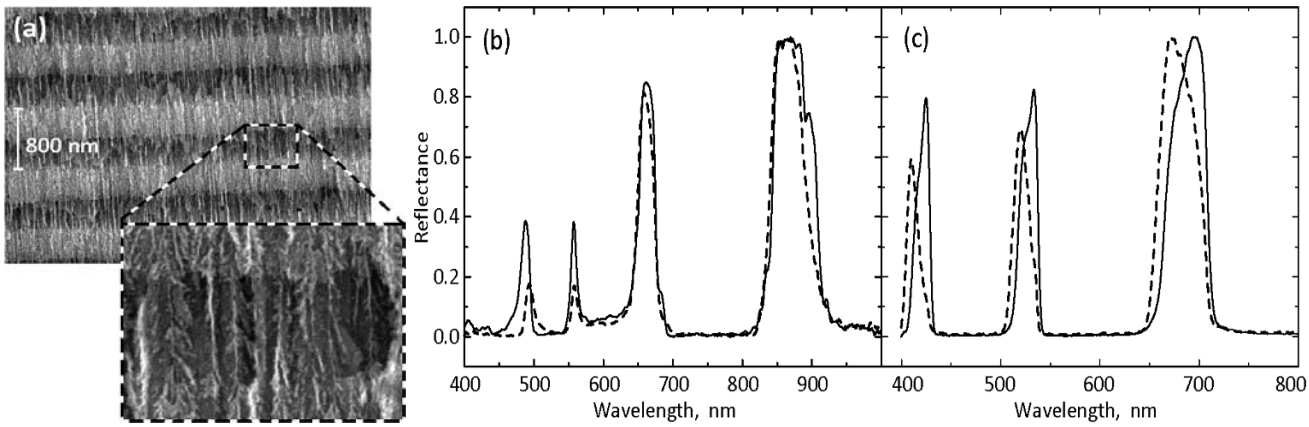

Fig. 2. Experimental sample – 1D porous silicon-based photonic crystal and SEM side view of the PhC (a) and the reflection spectra of the front side (solid curve) and the back side (dashed curve) of the PhC before (b) and after the annealing (c).

collinear second harmonic generated in the BBO was filtered by a pinhole and measured by an avalanche photodiode.

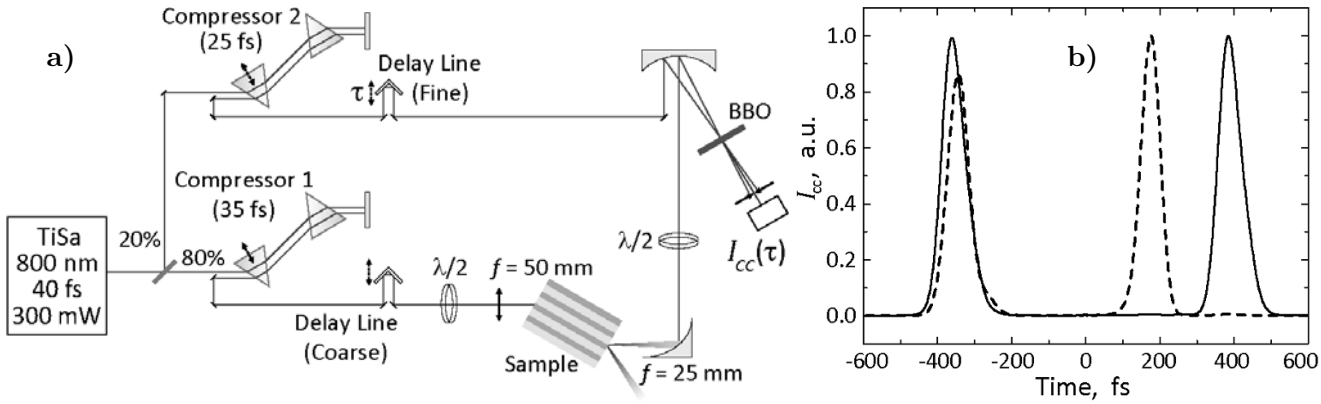

Fig. 3. Schematic view of the experimental set-up (a) and the cross-correlation functions measured for the *p*-polarized (solid curve) and *s*-polarized (dashed curve) incident pulses (b).

For the measurements of the diffraction-induced temporal splitting of short laser pulses, we used cross-correlation (CC) function measurements. The cross-correlation-function signal is given by $I_{\mathrm{CC}}(t') \propto \int_{-\infty}^{\infty} I_S(t) I_R(t+t')\,dt$, where $I_S(t)$ and $I_R(t)$ are the pulse intensities in the signal and reference arms, and t' is the delay time between them.

The parameters of the PhC sample were described in Sec. 2. The length of the sample in the direction of the light propagation was $z_0 = 2.4$ mm.

The cross-correlation functions obtained for the p and s polarizations of pulsed radiation are shown in Fig. 3 b. Time $t = 0$ corresponds to the calculated arrival time of a femtosecond pulse passed through a homogeneous effective medium (without spatial periodicity) of the same length z_0 and with the refractive index $n_{\mathrm{eff}} = (n_1 + n_2)/2$. The measured functions correspond to the two pulses outgoing the PhC, the temporal delay between them being $t_{12}^{(p)} = 746 \pm 2$ fs for the p-polarized incident radiation and $t_{12}^{(s)} = 518 \pm 2$ fs for the s-polarized one, while the amplitudes of split pulses are almost equal to each other. Therefore, the effect of diffraction-induced pulse splitting in photonic crystals at the Laue geometry is experimentally observed [12].

Noteworthy is that the splitting time t_{12} depends strongly on the polarization of the incident pulse — the splitting time increases nearly 1.5 times when the polarization is changed from s to p. The mechanisms underlying these effects are discussed in the next section.

5. Polarization Properties of the DIPS Effect

The polarization dependence of the dynamical Bragg diffraction effects originates from the structural anisotropy of 1D PhC. Equation (2) contains a part $\nabla \times \nabla \times \mathbf{E}(\mathbf{r}, t) = -\Delta \mathbf{E}(\mathbf{r}, t) + \nabla\big(\nabla \mathbf{E}(\mathbf{r}, t)\big)$, where $\Delta = (\partial^2/\partial x^2) + (\partial^2/\partial z^2)$ is the Laplace operator and $\nabla \mathbf{E} = -(\nabla \varepsilon)\varepsilon^{-1}\mathbf{E}$. The permittivity gradient $\nabla \varepsilon(x)$ can be large enough in a PhC with high refractive-index contrast $\Delta n = n_1 - n_2$; therefore, the field divergence $\nabla \mathbf{E} \neq 0$, and the plane electromagnetic wave is not transverse. It is more convenient to consider the magnetic field $\mathbf{H}(\mathbf{r}, t)$ instead of the electric field as it is transverse in a nonmagnetic

medium. Finally, we can write the wave equation as follows:

$$\Delta\mathbf{H} + \frac{\nabla\varepsilon(x)}{\varepsilon} \times \nabla \times \mathbf{H} - \frac{\varepsilon(x)}{c^2}\frac{\partial^2\mathbf{H}}{\partial t^2} = 0. \tag{4}$$

The second term determines the structural anisotropy of a periodic lattice. The solution of this equation is considered in detail elsewhere [15] and consists of a set of plane waves obeying the dispersion relation. Dispersion curves, isofrequency values of the z component of the wave vector depending on the detuning off the Bragg condition, are shown in Fig. 4 a. The corresponding calculated splitting times for s and p polarizations of the propagating pulses are given by

$$t_{12}^{(s)} = \frac{z\varepsilon_h}{c\sqrt{\varepsilon_0}}\left(1 - \frac{\sin^2\theta_B}{2\varepsilon_0}\right), \qquad t_{12}^{(p)} = \frac{z\varepsilon_h}{c\sqrt{\varepsilon_0}}\left(1 + 3\frac{\sin^2\theta_B}{2\varepsilon_0}\right). \tag{5}$$

This expression indicates that the splitting time for the p polarization in 1D photonic crystals is always larger as compared to the s polarization.

The measurements of the temporal pulse profiles were performed as the polarization of the incident radiation was changed continuously from p to s. This was made by a synchronous rotation of two half-wave plates shown in Fig. 3 a. The corresponding results are shown in Fig. 4 b. It can be seen that the pulse profile is switched continuously from the p polarization to the s polarization. For the intermediate polarization (tilted to 45° from the p polarization), the four pulses are observed at the exit of the crystal. Note that the Borrmann and anti-Borrmann pulses are not symmetric with respect to the time $t = 0$. This asymmetry of the peak times is caused by the material anisotropy of the porous fused-silica layers. It is known [34] that porous silicon and porous SiO_2 exhibit birefringence, i.e., they are uniaxial media with the optical axis parallel to the pores. The birefringence $|n_\mathrm{e} - n_\mathrm{o}|$ depends on the pore size of the sample: the greater the pore diameter and porosity, the greater the refractive index contrast. Figure 4 d shows the results of the analytic calculation of the pulse shapes for the two polarizations when the birefringence is taken into account. For the layers of low porosity, the refractive indices of $n_{1,\mathrm{o}} = 1.46$ and $n_{1,\mathrm{e}} = 1.45$ are considered. For the layers of high porosity, $n_{2,\mathrm{o}} = 1.35$ and $n_{2,\mathrm{e}} = 1.32$, respectively.

Thus, we observed the polarization dependence of the splitting time in the DIPS effect. It is associated with the structural anisotropy of the PhC lattice, which is proportional to the gradient of the dielectric function and rises with the refractive index contrast. In porous fused silica-based 1D PhCs, the polarization dependence is larger because of the second involved phenomenon – the variation of material birefringence between two types of the PhC layers.

6. Spatial Pulse Distribution inside the Photonic Crystals

The propagation direction of the laser pulse inside a PhC can be predicted by analyzing the dispersion curves. The normal vectors shown in Fig. 4 a denote the direction of pulse propagation, which depends on the angle of incidence. In the case of matching the Bragg condition ($\theta_B = 31°$), both Borrmann and anti-Borrmann pulses propagate along the z axis. When the angle of incidence is detuned from the Bragg condition, for instance, it is smaller (θ =30°), the Borrmann pulse should propagate in the direction with the negative projection on the x axis, while the anti-Borrmann pulse propagation direction will correspond to the positive one, as is shown in Fig. 5 d. At larger angles of incidence, the directions of propagation of the pulses change conversely (see Fig. 5 e).

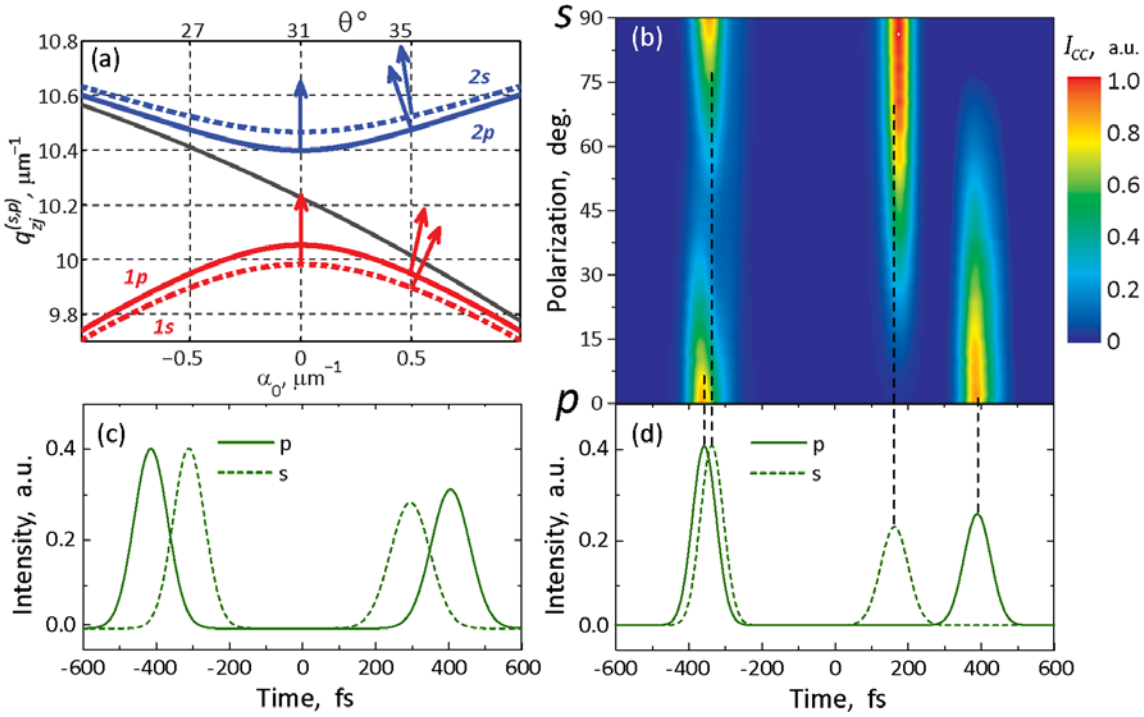

Fig. 4. Dispersion curves for Borrmann (red) and anti-Borrmann (blue) modes for different polarizations of incident pulses, where the arrows show the normal direction and the black curve corresponds to the pulse propagating in a uniform medium with $n_{\text{eff}} = (n_1 + n_2)/2$ (a). Experimentally measured temporal pulse profiles after passing the PhC for variable linear polarizations (b). Results of the analytical calculations of the temporal pulse profiles for isotropic PhC with $n_1 = 1.47$ and $n_2 = 1.32$ (c) and for anisotropic PhC with $n_{1,\text{o}} = 1.46$, $n_{1,\text{e}} = 1.45$, $n_{2,\text{o}} = 1.35$, and $n_{2,\text{e}} = 1.32$ (d).

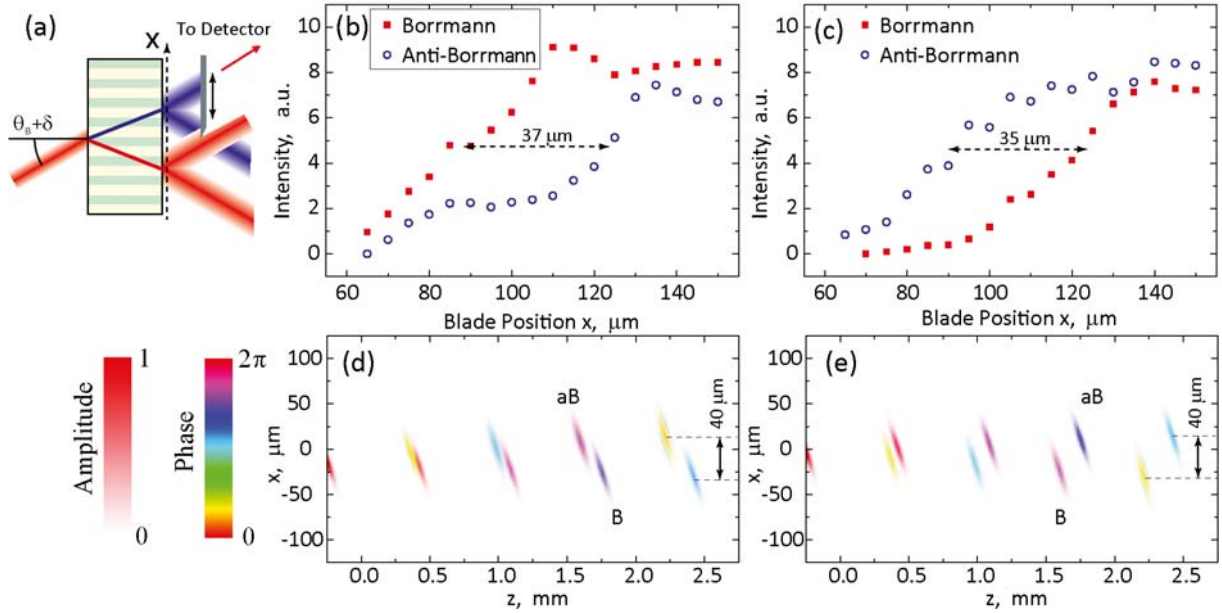

Fig. 5. Spatial shift of pulses in the DIPS effect. Scheme of the experiment (a), experimental dependences of the magnitude of the Borrmann and anti-Borrmann pulses on the blade position for the angles of incidence detuning $\delta = -1°$ (b) and $\delta = 0.9°$ (c), respectively, and calculated amplitudes of Borrmann and anti-Borrmann pulses propagating through a PhC for angles $\delta = -1°$ (d) and $\delta = 1°$ (e), respectively.

Therefore, the pulse positions in a PhC can be controlled by variation of the angle of incidence. We performed the experimental verification of this prediction as follows. A metal blade was situated close to the exit surface of the sample, the distance between them being approximately 10 μm. The blade could be moved parallel to the sample surface, as is shown schematically in Fig. 5,a. The sample was placed on a rotation mount to control the incident angle. Other parts of the set-up shown in Fig. 3 a remained unchanged. The Borrmann and anti-Borrmann pulses were resolved on the cross-correlation function of the beam passed through the sample. The aperture of the cross-correlation detector was large enough to get a signal at a spot of 150 μm of the exit surface.

Measured magnitudes of the Borrmann and anti-Borrmann pulses in the case of smaller angle of incidence (30°, Bragg detuning $\delta = \theta - \theta_B = -1°$) are shown in Fig. 5 b. While the blade moves along the rear surface of the sample in the positive direction of the x axis, it opens first the Borrmann pulse and second the anti-Borrmann pulse. This means that the Borrmann pulse propagates in a PhC at smaller x values as compared to the anti-Borrmann pulse, which correlates with the analytic predictions (Fig. 5 d). The distance between the pulses is 37 ± 5 μm. In the case of larger incident angle (32°, Bragg detuning $\delta = 1°$), conversely, the blade opens first the anti-Borrmann pulse and second the Borrmann pulse. The corresponding analytical distribution of the pulse field is shown in Fig. 5 e. The measured distance between the pulses is 35 ± 5 μm. The distance between the pulses calculated analytically is 40 μm in both cases.

Therefore, we show that the Borrmann and anit-Borrman pulses split spatially inside the PhC and can propagate in the opposite x directions depending on the detuning of the incident pulse off the Bragg condition.

7. Dynamical Diffraction of Phase-Modulated Pulses. Selective Pulse Focusing and Compression

As was mentioned above, the propagation direction of the Borrmann and anti-Borrmann pulses can be controlled by a proper choice of the angle of incidence on a PhC. The entire pulse propagates in the direction corresponding to the normal to the dispersion curve (see Fig. 4 a) and depending on the detuning angle out of the Bragg condition $\delta = \theta - \theta_B$. If a short pulse is spatially or temporally broadened by the phase modulation (chirp), different "parts" of the pulse can be controlled independently in the same way. For example, a spatially phase-modulated (focused) pulse will undergo the following transformation. Its central part matches the Bragg condition and thus propagates directly. One side part of the pulse has a positive detuning δ and consequently the propagation direction of a part of the Borrmann pulse has the positive projection on the x axis and the negative one for the anti-Borrmann pulse. The other side part of the initial pulse has negative detuning and thus propagates in the negative direction with respect to the x axis for the Borrmann pulse. Consequently, the side parts of the Borrmann pulse move toward each other in the transverse direction and this pulse will squeeze (focusing). Similarly, the anti-Borrmann pulse stretches in the transverse direction (defocusing). Therefore, one expects that the Borrmann and anti-Borrmann pulses can be selectively focused or defocused depending on the spatial phase modulation.

In a similar way, the temporal phase modulation (chirp) of the incident pulse should cause squeezing and broadening of pulses in the time domain; in this case, one may expect pulse compression and decompression. These effects were theoretically predicted [14] and experimentally observed [35].

Now we consider a phase-modulated pulse

$$A_{in}(x,t) = A_0 exp\left[-\left(\frac{x\cos\theta}{r_0}\right)^2(1-i\sigma) - \left(t-\frac{x\sin\theta}{c}\right)^2\frac{1-i\beta}{\tau_0^2}\right], \tag{6}$$

where r_0 and τ_0 are the radius and duration of a nonmodulated pulse, θ is the angle of incidence, c is the speed of light, and σ and β are the spatial and temporal phase modulation parameters. The calculation of the field distribution during the pulse propagation within a PhC is shown in Fig. 6.

Figure 6 shows transformations of the Borrmann and of the anti-Borrmann pulses during their propagation in a PhC for different spatial and temporal phase-modulation parameters. It can be seen that a spatially phase-modulated initial pulse ($\sigma = \pm 15$) splits into two pulses, one of which is focused and the other defocused, as shown in Fig. 6 a and b. In the case of negative modulation ($\sigma = -15$, initial beam is focused), the Borrmann pulse is focused, while the anti-Borrmann is defocused. The pulses are "rotated" in the spatial domain due to the focusing mechanism described above — the initial pulse inside a PhC is stretched or squeezed along the x direction. The spatial phase modulation of split pulses can be seen in Fig. 6 c, where one sees that the central part of the pulse is stretched or squeezed. The temporal phase modulation of the incident pulse leads to temporal compression and decompression of split pulses, as shown in Fig. 6 d and e.

8. Optical Switching at a Pendular Effect

As was discussed earlier, when the light propagates in a PhC at the Laue geometry close to the Bragg angle, two modes of the electromagnetic field, Borrmann and anti-Borrmann ones, are excited. Noteworthy is that the field of each of these modes is a superposition of two plane waves, transmitted and diffracted ones (7). For the case of s polarization, the electric field of a mode is given by

$$E_j^{(s)}(x,z,t) = e_y \exp\big(-i\omega t + iq_{zj}^{(s)}z\big)\big(E_{hj}^{(s)}\exp\left(i(k_x-h)x\right) + E_{0j}^{(s)}\exp\left(ik_x x\right)\big), \quad j=1,2. \tag{7}$$

where the superscript s stands for the s polarization, and indices 1 and 2 denote the mode number. An analogous expression is valid for the H field in the case of p polarization.

Close to the Bragg angle, the field of the Borrmann mode is localized predominantly in the PhC layers with low refractive index, and vice versa for the anti-Borrmann mode. This is due to the relations for the amplitudes $E_{01}^{(s)} \approx iE_{h1}^{(s)}$ and $E_{02}^{(s)} \approx -iE_{h2}^{(s)}$. So different spatial localization leads to different dispersion relations for these modes, as is illustrated by analytic calculations; see Fig. 4 a. The anti-Borrman mode has a larger z component of the wave vector as compared to that of the Borrmann mode. The mode energy propagates toward the group velocity vector, which is perpendicular to the dispersion curve. As the dispersion curve is convex for the Borrmann mode and concave for the anti-Borrmann one, the group velocity vectors of these modes are not parallel in the general case.

The interference of the Borrmann and anti-Borrmann modes leads to optical beating, which is due to different z components of the modes. The total s-polarized field inside a PhC is given by

$$E^{(s)}(x,z,t) = E_0^{(s)}(x,z,t) + E_h^{(s)}(x,z,t), \tag{8}$$

where $E_g^{(s)}(x,z,t) = e_y \exp\big(-i\omega t + i(k_x-g)x\big)\big(E_{g1}^{(s)}\exp\left(iq_{z1}^{(s)}z\right) + E_{g2}^{(s)}\exp\left(iq_{z2}^{(s)}z\right)\big)$, with $E_{gj}^{(s)}$ being the waves amplitudes, and $g = 0,\ h$. The spatial period of beating is given by the extinction length $\Lambda = 2\,\Lambda_{\text{ext}}$

determined as [10]

$$\Lambda_{\text{ext}}(\Delta n, \lambda, C_{s,p}) = \frac{\pi}{\left|q_{0z}^{(1)} - q_{0z}^{(2)}\right|} = \lambda_0 \frac{(n_e^2 - \sin^2\theta)^{1/2}}{2C_{s,p}|\chi_h|}.$$

The extinction length depends on the wavelength and polarization of the light and increases with the refractive index contrast. On account of the amplitude relations $E_{01}^{(s)} \approx E_{02}^{(s)}$ and $E_{h1}^{(s)} \approx -E_{h2}^{(s)}$, the beatings of the transmitted and diffracted waves are shifted on the extinction length Λ_{ext}, so the maximum of the transmitted wave corresponds to the minimum of the diffracted one, and vice versa. This can be considered as an energy exchange between the transmitted and diffracted waves inside a PhC, known as the pendular effect [11].

Such beatings inside PhCs occur also at detuning from the Bragg angle until the beams of the Borrmann and anti-Borrmann modes do not spatially diverge. The pendular effect exists not only for a monochromatic beam but for a wave package, as well. In this case, relation (8) should be considered for one spectral field component only; the total field is given by a frequency integration of (8). As was discussed above [14], for a sufficiently short laser pulse or a sufficiently long PhC, the pulse splitting effect appears. Each of pulses is formed by only Borrmann or anti-Borrmann mode. Therefore, the pendular effect may occur at the first stage of pulse splitting, when the two pulses are overlapped.

Inside a PhC, two transmitted waves with wave vectors $\mathbf{q_{01}}$ nd $\mathbf{q_{02}}$ propagate in slightly different directions, but, after refraction at the PhC exit edge, they become co-directional and only one plane wave in transmitted direction is formed. Analogously, one diffracted wave arises in free space from diffracted waves with $\mathbf{q_{h1}}$ and $\mathbf{q_{h2}}$. Transmitted and diffracted waves in free space have the wave vectors $\mathbf{k}$ and $\mathbf{k} - \mathbf{h}$. The amplitudes of these waves in a free space can be considered as a result of the interference of two co-directional refracted waves. Therefore, the intensities of the output transmitted and diffracted beams are not equal and depend on the phase incursion of the waves inside the PhC. If the PhC length L is equal to the even number of the extinction length $L = 2n\Lambda_{\text{ext}}$, the diffracted wave near the PhC exit edge has a minimum, while the transmitted waves interfere constructively; see (8). In this case, the light energy is concentrated in the transmitted beam only. If $L = (2n+1)\Lambda_{\text{ext}}$, the total energy propagates in the diffracted beam.

The pendular effect is a way to control the light flow by changing the extinction length, which can be realized by changing the polarization, wavelength, and the refractive index contrast. We carried out a calculation of the light propagation through a PhC slab under Bragg diffraction in the Laue geometry by means of the dynamical diffraction theory. In our model, we considered the PhC with parameters described in Sec. 2 and length $L = 18.36$ μm.

In Fig. 7 a, we show the light propagation through such a PhC for the s and p polarizations. The light with 800 nm wavelength falls on a PhC at Bragg angle of 30° from the left bottom corner and partially reflects. Inside the PhC, beating of field occurs. The PhC parameters are chosen as $L = 4\Lambda^{(s)} = 3\Lambda^{(p)}$. Therefore, the s-polarized incident light propagates in the transmitted direction, and the p-polarized light in the diffracted one. In other words, this device works as a compact polarizing beam splitter. Due to the high refractive index, the extinction length is sufficiently small, $\Lambda_{\text{ext}}^{(s)} \approx 4.6$ μm and $\Lambda_{\text{ext}}^{(p)} \approx 6.2$ μm.

The pendular effect can be useful for splitting light beams with different wavelengths. We observed experimentally the pendular effect for different wavelengths. We carried out our experiments at the same sample as in the pulse splitting experiments. A tunable OPO system with a pulse repetition rate of 10 Hz and a pulse duration of 10 ns was used as a laser source. Prior to impinging on the PhC, the light beam was spatially filtered. The p or s-polarized radiation focused by a 3 cm lens falls on the PhC edge

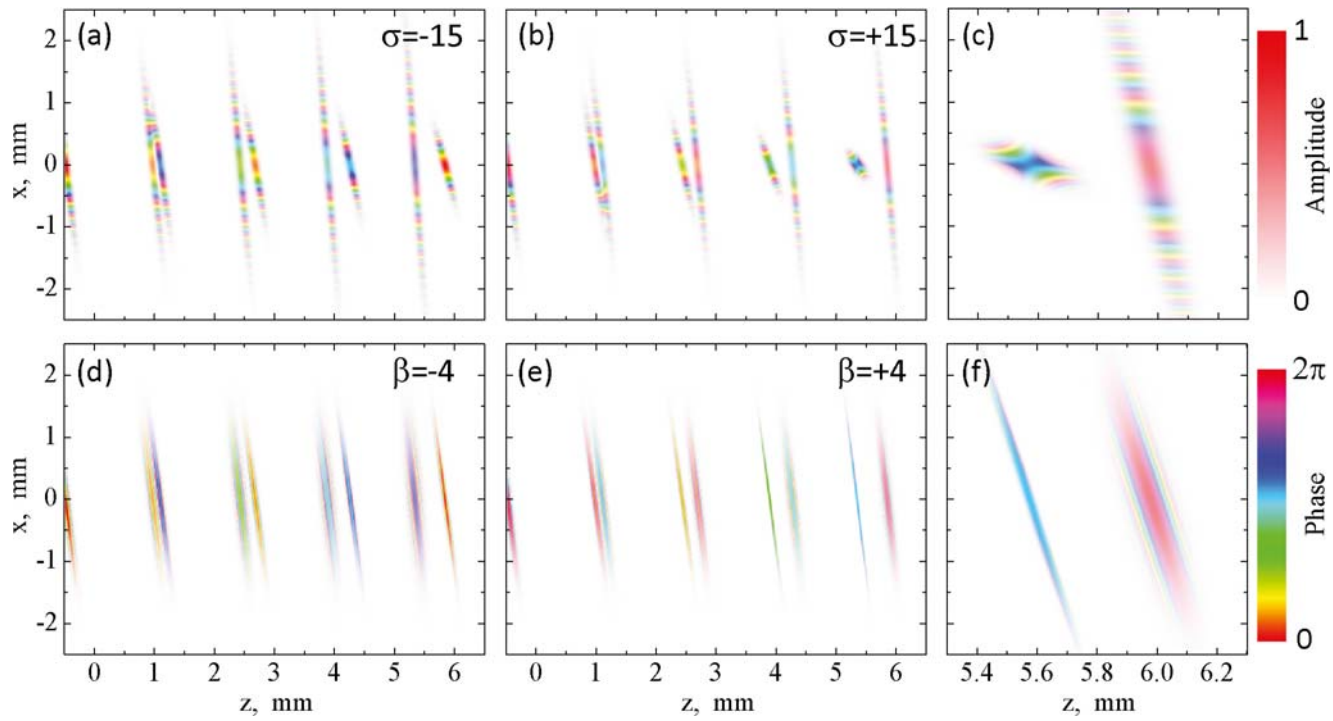

Fig. 6. Analytically calculated spatial distribution of complex field amplitudes $A_0 + A_h$ of diffracted phase-modulated pulses propagating through a PhC in the Laue geometry. Parameters of the modulation are: $\sigma = -15$ and $\beta = 0$ (a), $\sigma = +15$ and $\beta = 0$ (b), $\sigma = 0$ and $\beta = -4$ (d), and $\sigma = 0$ and $\beta = +4$ (e). Panels (c) and (f) show the last pairs of the pulse shown in panels (b) and (e) in a smaller scale.

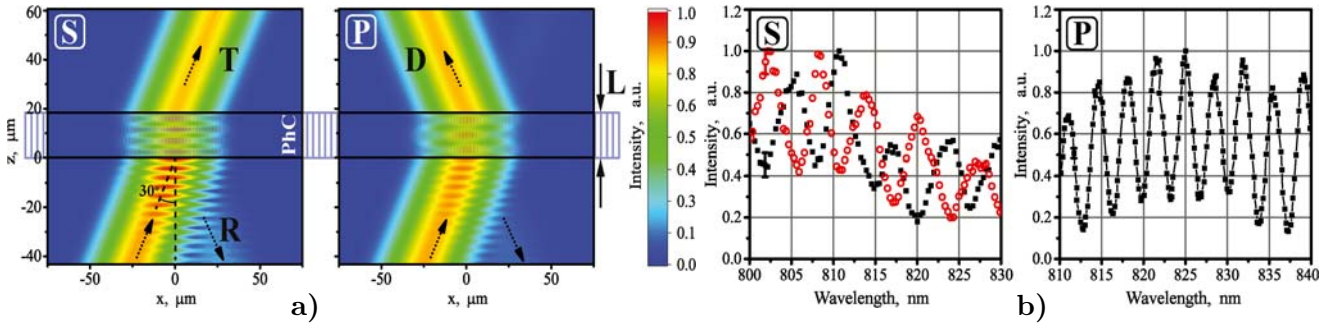

Fig. 7. Intensity distributions of light under Bragg diffraction in a PhC in the Laue geometry (a) for the *s*-polarized light (left) and the *p*-polarized light (right) for PhC layer thicknesses $d_1 = d_2 = 400$ nm, PhC length $L = 18.36\ \mu\text{m} = 4\Lambda^{(s)} = 3\Lambda^{(p)}$, and refractive indices $n_1 = 1.32$ and $n_2 = 1.48$. Here, light falls from the left-bottom corner, and R, T, and D are reflected, transmitted, and diffracted beams, respectively. The spectral dependence (b) of the intensity in transmitted (○) and diffracted (■) beams at *s*-polarized laser radiation (left) and *p*-polarized laser radiation (right).

at Bragg angle of 30°. Two beams propagating after coming out from the PhC in the transmitted and diffracted directions were observed. Their intensities were measured by a silicon photodiode using gated electronics.

The spectral dependences of the outgoing light intensity are shown in Fig. 7 b. It exhibits oscillations for the *s* and *p* polarizations of both transmitted and diffracted beams. However, the period of oscillations is significantly smaller for the *p*-polarized light than for the *s*-polarized light, $\Delta\lambda_p = 3.56 \pm 0.01$ nm and

$\Delta\lambda_s = 6.1 \pm 0.1$ nm. The intensity oscillations are in antiphase for the T and D beams, which reveals the energy exchange between them. It was estimated that, in our PhC, the energy exchange between the transmitted and diffracted beams occurs for more than 200 times, $L \approx 200\,\Lambda_{\text{ext}}^{(s)}$. This quantity is explained by the large PhC length, $L \approx 1$ mm, and the high refractive index contrast; the PhC sample is diffraction-thick ($N = L/\Lambda_{\text{ext}} \gg 1$).

9. Summary

We studied the effects accompanying the dynamical Bragg diffraction of light in 1D photonic crystals. We predicted theoretically and observed experimentally the effect of diffraction-induced pulse splitting. We fixed a pronounced polarization dependence of the splitting time and explained it as originating from the two effects, the structural anisotropy of the PhC lattice and the material anisotropy of the PhC layers. Also we evaluated the relative contributions of these effects.

We demonstrated that the propagation of the temporally split pulses within a PhC were angle dependent and could therefore be controlled. We calculated analytically the dependence of the intensity of a pulse passed through a PhC on the second-order spatial phase modulation (SPM) of the incident pulse and showed both experimentally and theoretically that the pulses, split due to the diffraction-induced splitting effect, can be selectively focused or defocused depending on the spatial phase modulation of the incident light pulse.

We observed the pendular effect, that is, the periodic energy switching between the transmitted and diffracted modes in a PhC, in the case of a diffraction-thick PhC with a length of about a hundred of switching periods. We demonstrated the spectral and polarization-induced switching of the light beams outgoing from the porous silicon-based 1D photonic crystal for the Bragg conditions in the Laue diffraction scheme.

Acknowledgments

This work was partially supported by the Russian Foundation for Basic Research under Projects Nos. 13-02-00300, 14-29-07197, and 14-02-31770 and the Scholarship of the President of the Russian Federation under Project No. SP- 3372.2015.5.

References

1. K. Busch, G. von Freymann, S. Linden et al., *Phys. Rep.*, **444**, 101 (2007).
2. E. M. Purcell, H. C. Torrey, and R. V. Pound, *Phys. Rev.*, **69**, 37 (1946).
3. P. Lodahl, A. F. Van Driel, I. S. Nikolaev, et al. *Nature*, **430**, 654 (2004).
4. Hatice Altug and Jelena Vucković, *Appl. Phys. Lett.*, **86**, 111102 (2005).
5. H. Gersen, T. J. Karle, R. J. P. Engelen, et al., *Phys. Rev. Lett.*, **94**, 073903 (2005).
6. T. Dolgova, A. Maidykovski, M. Martemyanov, et al., *Appl. Phys. Lett.*, **81**, 2725 (2002).
7. J. F. McMillan, X. Yang, N. C. Panoiu, et al., *Opt. Lett.*, **31**, 1235 (2006).
8. M. Inoue, K. Arai, T. Fujii, and M. Abe, *J. Appl. Phys.*, **83**, 6768 (1998).
9. K. Inoue and K. Ohtaka, *Photonic Crystals: Physics, Fabrication and Applications*, Springer (2013).
10. V. A. Bushuev, B. I. Mantsyzov, and A. A. Skorynin, *Phys. Rev. A*, **79**, 053811 (2009).

11. M. L. Calvo, P. Cheben, O. Martínez-Matos, et al., *Phys. Rev. Lett.*, **97**, 084801 (2006).
12. S. E. Svyakhovskiy, V. O. Kompanets, A.I. Maydykovskiy, et al., *Phys. Rev. A*, **86**, 013843 (2012).
13. I. Shutov, I. Ozheredov, A. Shumitski, and A. Chirkin, *Opt. Spectrosc.*, **105**, 79 (2008).
14. A. A. Skorynin, V. A. Bushuev, and B. I. Mantsyzov, *J. Exp. Theor. Phys.*, **115**, 56 (2012).
15. S. E. Svyakhovskiy, A. A. Skorynin, V. A. Bushuev, et al., *J. Opt. Soc. Am. B*, **30**, 1261 (2013).
16. F. Lederer, G. I. Stegeman, D. N. Christodoulides, et al., *Phys. Rep.*, **463**, 1 (2008).
17. N. K. Efremidis, S. Sears, D. N. Christodoulides, et al., *Phys. Rev. E*, **66**, 046602 (2002).
18. F. Verluise, V. Laude, Z. Cheng, et al., *Opt. Lett.*, **25**, 575 (2000).
19. G. D. Marshall, M. Ams, and M. J. Withford, *Opt. Lett.*, **31**, 2690 (2006).
20. J. Scrimgeour, D. N. Sharp, C. F. Blanford, et al., *Adv. Mater.* **18**, 1557 (2006).
21. M. Miyake, Y. Chen, P. V. Braun, and P. Wiltzius, *Adv. Mater.* **21**, 3012 (2009).
22. P. Ni, P. Dong, B. Cheng, et al., *Adv. Mater.*, **13**, 437 (2001).
23. D. Wang and H. M. Hwald, *Adv. Mater.*, **16**, 244 (2004).
24. P. Jiang and M. J. McFarland, *J. Am. Chem. Soc.*, **126**, 13778 (2004).
25. L. Pavesi, *Nuovo Cim.*, **20**, 1 (1997).
26. A. V. Tikhonravov, M. K. Trubetskov, and G. W. DeBell, *Appl. Opt.*, **35**, 5493 (1996).
27. R. Geiss, S. Saravi, A. Sergeyev, et al., *Laser Opt.*, **40**, 3 (2015).
28. S. E. Svyakhovskiy, A. I. Maydykovsky, and T. V. Murzina, *J. Appl. Phys.*, **112**, 013106 (2012).
29. A. Uhlir, *Bell Syst. Tech. J.*, **35**, 333 (1956).
30. V. Lehmann and U. Gösele, *Appl. Phys. Lett.*, **58**, 8 (1991).
31. R. L. Smith and S. D. Collins, *J. Appl. Phys.*, **71**, 8 (1992).
32. E. Lorenzo, C. J. Oton, N. E. Capuj, et al., *Physica Status Solidi (c)*, **2**, 3227 (2005).
33. B. E. Deal and A. Grove, *J. Appl. Phys.*, **36**, 3770 (1965).
34. L. Golovan, D. Ivanov, V. Melnikov, et al., *Appl. Phys. Lett.*, **88**, 241113 (2006).
35. S. E. Svyakhovskiy, A. A. Skorynin, V. A. Bushuev, et al., *Opt. Exp.*, **22**, 31002 (2014).